J. Eng. Technol. Sci., Vol. 53, No. 1, 2021, 210101

Global Inversion of Grounded Electric Source Time-domain Electromagnetic Data Using Particle Swarm Optimization

Cahyo Aji Hapsoro[1], Wahyu Srigutomo[1,*], Acep Purqon[1], Warsa Warsa[2], Doddy Sutarno[1] & Tsuneomi Kagiyama[3,4]

[1]Physics of Earth and Complex System, Faculty of Mathematics and Natural Sciences, Institut Teknologi Bandung, Jalan Ganesa 10, Bandung 40132, Indonesia
[2]Applied Geophysics and Exploration, Faculty of Mining and Petroleum Engineering, Institut Teknologi Bandung, Jalan Ganesa 10, Bandung 40132, Indonesia
[3]Aso Volcanological Laboratory, Institute for Geothermal Sciences, Graduate School of Science, Kyoto University, 3028 Sakanashi, Ichinomiyamachi, Aso, Kumamoto 869-2911, Japan
[4]Aso Volcano Museum, 1930-1, Akamizu, Aso, Kumamoto 869-2232, Japan
*E-mail: wahyu@fi.itb.ac.id

Highlights:

- The PSO inversion scheme was applied to the grounded wire TDEM method to infer subsurface resistivity models.
- The forward modeling part was expressed in the Laplace domain, while the transformation into the time-domain was conducted using the Gaver-Stehvest method.
- The inversion scheme was tested on noise-free and noisy synthetic data to evaluate the accuracy of the scheme and was then applied to field data recorded at two stations in a volcanic-geothermal region.
- The inversion scheme gave an excellent fit between the observed data and the calculated data.

Abstract. Global optimization inversion of grounded wire time-domain electromagnetic (TDEM) data was implemented through application of the particle swarm optimization (PSO) algorithm. This probabilistic approach is an alternative to the widely used deterministic local-optimization approach. In the PSO algorithm, each particle that constitutes the swarm epitomizes a probable geophysical model comprised by subsurface resistivity values at several layers and layer thicknesses. The forward formulation of the TDEM problem for calculating the vertical component of the induced magnetic field is first expressed in the Laplace domain. Transformation of the magnetic field from the Laplace domain into the time domain is performed by applying the Gaver-Stehfest numerical method. The implementation of PSO inversion to the TDEM problem is straightforward. It only requires adjustment of a few inversion parameters such as inertia, acceleration coefficients and numbers of iteration and particles. The PSO inversion scheme was tested on synthetic noise-free data and noisy synthetic data as well as to field data recorded in a volcanic-geothermal area. The results suggest that the PSO inversion scheme can effectively solve the TDEM 1D stratified earth problem.

Received January 23rd, 2020, Revised July 25th, 2020, Accepted for publication September 17th, 2020.
 ISSN: 2337-5779,
DOI: 10.5614/j.eng.technol.sci.2021.53.1.1

Keywords: *horizontal electric dipole; particle swarm optimization; resistivity; electromagnetic time-domain; synthetic and field data; volcanic-geothermal area.*

1 Introduction

The time-domain electromagnetic (TDEM) method measures the magnetic field attenuation with respect to time caused by the generation of time-varying secondary EM fields in the subsurface as a response to an abrupt current cancelation in a grounded wire transmitter. Forward formulation of TDEM for one-dimensional (1D) stratified earth has been comprehensively reviewed in [1-3]. Domain transformation from frequency to time for the TDEM method has been carried out by several authors, either directly using the Fourier transform or through the Laplace transform. In the latter case, the TDEM forward formulation is first expressed in the Laplace domain.

The realization of TDEM response calculations can be conducted through several methods. For example, Qi, *et al*. [4] used the so-called temporal interpolation and convolution (TIC) method, which is faster than the fast Fourier transform (FFT) method yet has comparable accuracy [4-6] for dipole-dipole and central loop configurations. Newman, *et al.* [7] and Farquharson and Oldenburg [8] used the digital filter method to calculate the transient responses from a vertical magnetic dipole (VMD). Mitsuhata, *et al*. [9] implemented the Gaver-Stehvest method [10-12] to calculate the transient responses for the long-offset transient EM (LOTEM) method. The same method was also used by Srigutomo, *et al.* [13] for a horizontal electric dipole (HED) configuration. The FFT method is well perceived because of its high accuracy at the expense of computation time, as can be seen in the calculation of transient responses for VMD cases [4,14]. The Gaver-Stehfest method is a numerical method for calculating the inverse Laplace transform to obtain the expression of the transient responses. This method provides accurate results when implemented to a transform with known analytical form [10] and converges to a function of bounded variation [12]. This method provides faster calculation than digital-filter and FFT methods [12,15]. The digital filter method involves more functions and steps than the Gaver-Stehvest method and thus requires longer computation time [15,16].

The TDEM method has been widely applied in geophysical explorations. Fitterman & Stewart [17] used the VMD configuration for groundwater investigation. Zhdanov & Pavlov [18] implemented a similar configuration for interpreting the subsurface structure with both electrical conductivity and magnetic permeability inhomogeneities. Qi, *et al.* [19] employed an airborne TEM system using a pair of transmitter-receiver coil antennas to investigate the subsurface structure taking into account the effects of the antennas' attitude changes. Blatter, *et al*. [20] used an airborne TEM configuration to image a

subglacial hydrology structure in Antarctica. Newman, *et al*. [21] used a central loop to study the thicknesses of the conductive overburden and depth to the sedimentary structure beneath a volcanic area. Asten [22] applied a large square loop transmitter and an in-loop receiver coil to delineate a coal seam based on conductivity contrast, while Haber, *et al.* [23] used the same configuration to investigate a Cu-Zn massive sulphide deposit. Mitsuhata, *et al*. [9] used the long offset transient electromagnetic (LOTEM) method, utilizing a grounded wire transmitter to study the resistivity structure beneath an oil and gas field. Kanda, *et al.* [24] used a grounded wire transmitter to observe the conductivity variation in a high-seismicity area. Gunderson, *et al*. [25] applied the same transmitter system to depict responses for a conductive sediment below a resistive volcanic area. Using the same configuration, Srigutomo, *et al*. [13] conducted a resistivity survey to confirm the presence of an extensive water-saturated layer beneath a volcanic area. Srigutomo, *et al*. [26] applied a grounded wire for benchmarking the resistivity structure of an area before CO_2 injection in a carbon capture and sequestration (CCS) study in Indonesia. In surveys that use a grounded wire transmitter, when the transmitter-receiver offset is large we can approximate the transmitter as a dipole source or an HED [13,24,25].

The most important step in the TDEM method is the numerical interpretation scheme used to extract information of the resistivity structure in the subsurface from the data measured at the surface, known as inversion. TDEM inversion is a non-linear problem dictated by the relation between the data and the model parameters. Non-linear inversion schemes can be broadly divided into deterministic and non-deterministic approaches. Some deterministic inversion schemes for solving TDEM inversion are the Levenberg-Marquardt [9] and smoothness-constrained inversion or Occam [13] methods. The non-deterministic methods are implemented by incorporating statistical approaches, such as the Bayesian [20], Akaike's Bayesian Information Criterion (ABIC) [9], and several approaches that utilize global optimization procedures.

The global optimization approach is an appropriate alternative to accommodate situations where there are many local minima in the objective function due to the probabilistic framework [27]. In the global optimization approach, the inverse problem solution is sought by employing a global search to obtain the absolute minimum objective function [28]. In geophysical applications, the non-uniqueness of the inversion solution makes the use of an optimization approach based on evolutionary algorithms such as particle swarm optimization (PSO) extremely challenging [29]. PSO is a stochastic evolutionary computation technique applied to optimization inspired by the behavior of a group consisting of individuals in nature, such as bird flocks and fish schools [30]. Previously, the behavior of animal movement in nature has been observed and computationally modeled by [31-33], where the aggregate motion of a bird flock consisting of

many interacting birds is represented by a motion of particle system. In the PSO algorithm, each particle is defined as an artificial bird that symbolizes a probable solution or model of the optimization inversion problem. The best position of the group of particles represents the best fit between the observed and the calculated data [34,35]. Ref. [36] used a damping factor and a cooperative mechanism for quickly searching the solutions residing between local-oriented swarms and global-oriented swarms. A damping factor and a cooperative mechanism are applied during the position updating step to find the best swarm position.

In geophysical inversion applications, the PSO algorithm has shown good performance in terms of global optimization ability, convergence rate, and robustness. PSO has been applied to direct current (DC) resistivity methods [37,38], seismic [39-41], streaming-potential [27], magnetic [33,42], gravity [43-45], airborne EM [46], AMT and MT data [29], and self-potential [47]. Furthermore, it has also been successfully used for an artificial neural network [48], reservoir characterization [49], and for big data research [50]. Global optimization using the PSO method can also be effectively applied to DC and TDEM studies [29]. VMD-TDEM inversion using global optimization has previously been carried out by [51], who applied and compared the PSO method with the genetic algorithm (GA) method. They utilized a central-loop configuration and solved the forward modeling part using Born approximation. Their results revealed that the PSO approach provides better and faster convergence compared to the GA method.

In previous decades, TDEM data inversion studies have been carried out with deterministic methods to determine the best fit value between observed and predicted data related to solutions at local minima. Currently, implementation of non-deterministic methods for solving the TDEM inversion problem are carried out increasingly by seeking solutions at global minima. This paper discusses the application of the PSO approach to the HED-TDEM inverse problem, where the forward modeling part is expressed in the Laplace domain and the transformation into the time-domain is conducted through the Gaver-Stehfest method. The inversion scheme was first applied to both noise-free and noisy synthetic data to investigate its performance. To check the applicability of the inversion scheme in a real application, the scheme was used to invert a resistivity structure from TDEM data measured in a volcanic environment.

2 Forward Modeling

2.1 Magnetic Field from the HED Source

The time-domain electromagnetic fields generated by a time-varying source current in a grounded wire or dipole are expressed as follows:

$$\nabla \times \mathbf{h}(\mathbf{r},t) = \sigma(\mathbf{r})\mathbf{e}(\mathbf{r},t) + \mathbf{j}_s(\mathbf{r},t), \tag{1}$$

$$\nabla \times \mathbf{e}(\mathbf{r},t) = -\mu_0 \frac{\partial \mathbf{h}(\mathbf{r},t)}{\partial t}, \tag{2}$$

where **h** is the intensity of magnetic field (H/m), **e** is the electric field intensity (V/m), μ_0 is the permeability of magnetic material (4π x10^{-7} F/m), and σ is the conductivity of the material in the subsurface (S/m). $\mathbf{j}_s$ (A/m^2) is the current distribution generated by an HED that is localized at $r = r_0$. For a cut-off current distribution at $t = t_0$ it is expressed as:

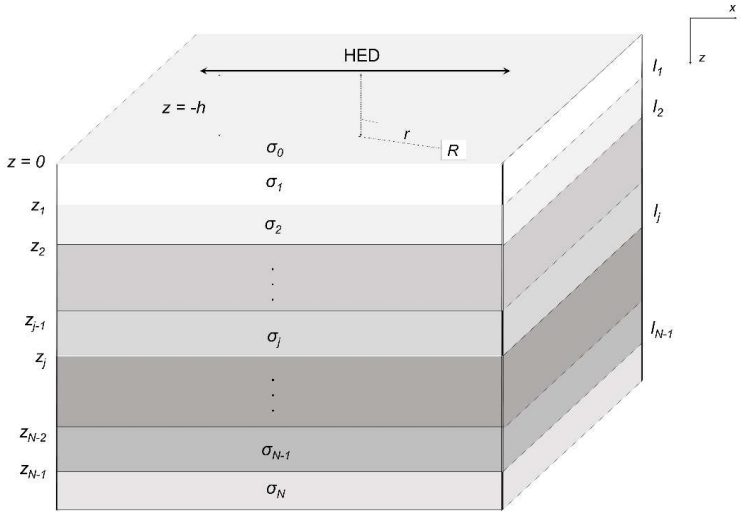

Figure 1 The layered earth model used in this work; zj is the depth to the j-th bottom layer, σj is the conductivity and lj is the thickness of the j-th layer.

$$\mathbf{j}_s(\mathbf{r},t) = I \cdot \delta(r - r_0) \cdot \left[1 - \mathrm{H}(t - t_0)\right], \tag{3}$$

where I is the current intensity (A) and H(t) is the Heaviside function.

In practice, it is more convenient to apply the Laplace transform than the Fourier transform due to the simplicity of the formulation [13]. The expression of $i\omega$ in the frequency domain is substituted by s. Then, we substitute expression $i\omega$ with s, the variable of the Laplace domain. This transformation is intended to avoid source singularity in time [13,15]. Eqs. (1) and (2) then become

$$\nabla \times \mathbf{H} = \sigma \mathbf{E} + \mathbf{J}_s, \tag{4}$$

$$\nabla \times \mathbf{E} = -s\mathbf{B}. \tag{5}$$

For simplicity, the conductivity is assumed to vary only vertically in the z direction. The earth consists of N layers of conductivity, with a constant conductivity for each layer. The HED source with current moment Idx is placed at $z = -h$, where dx denotes the length of the dipole. In the i-th layer, where $z_{i-1} < z < z_i$ (Figure 1), which is a free source area, Eqs. (4) and (5) become

$$\nabla \times \mathbf{H}_i = \sigma_i \mathbf{E}_i , \tag{6}$$

$$\nabla \times \mathbf{E}_i = -s\mathbf{B}_i . \tag{7}$$

(Kaufman & Keller, 1983) used vector potential $\mathbf{A}$ (A/m^2) for the expression of the magnetic field, such that

$$\mathbf{H}_i = \nabla \times \mathbf{A}_i . \tag{8}$$

Substituting Eq. (8) into Eq. (7), we obtain

$$\nabla \times \left(\mathbf{E}_i + \mu_0 s \mathbf{A}_i \right) = 0 . \tag{9}$$

The electric field can be expressed by introducing an arbitrary scalar potential U:

$$\mathbf{E}_i = -\mu_0 s \mathbf{A}_i - \nabla U_i . \tag{10}$$

From Eqs. (6) and (10) and using vector calculus identity, we obtain

$$\nabla \times \mathbf{H}_i = \nabla \times \nabla \times \mathbf{A}_i = \nabla \nabla \cdot \mathbf{A}_i - \nabla^2 \mathbf{A}_i = -\mu_0 s \sigma_i A_i - \sigma_i \nabla U_i \tag{11}$$

and by defining the gauge condition as

$$\nabla \cdot \mathbf{A}_i = -\sigma_i U_i , \tag{12}$$

and applying it to Eq. (11) we get:

$$\left(\nabla^2 + k_i^2 \right) A_i = 0 \tag{13}$$

where $k^2 = -\mu_0 s \sigma_i$. In this problem, we utilize two axes of symmetry: one is the dipole direction axis and the other one is the direction in change in the conductivity (the vertical direction in the 1D earth). Consequently, we can define that the y component of the potential vector equals zero:

$$A_i = \left(A_{x_i}, 0, A_{z_i} \right). \tag{14}$$

Therefore, we have the following two components of the vector potential:

$$\left(\nabla^2 + k_i^2 \right) A_{x_i} = 0 , \tag{15}$$

$$\left(\nabla^2 + k_i^2\right) A_{z_i} = 0\,. \tag{16}$$

By using the definition of the triple spatial Fourier transform pairs [52] and expressing the transform of $\nabla^2\mathbf{A} + k^2\mathbf{A} = -\mathbf{J}_e^S$, where $\mathbf{J}^S{}_e = i\omega\mathbf{P}^S$ and $\mathbf{P}$ is the polarization vector, and applying the Fourier transform derivative property, we obtain

$$\tilde{\tilde{\mathbf{A}}} = \tilde{\tilde{G}}\tilde{\tilde{\mathbf{J}}}\,, \tag{17}$$

where $\tilde{\tilde{\mathbf{A}}}$ and $\tilde{\tilde{\mathbf{J}}}$ are the expressions of the potential vector and current density in the wave number domain, respectively, and

$$\tilde{\tilde{G}} = \frac{1}{-k_x^2 - k_y^2 - k_z^2 + k^2} \tag{18}$$

is the Green's function Fourier transform.

In the space domain, Green's function satisfies

$$\nabla^2 G + k^2 G = -\delta(x)\delta(y)\delta(z)\,, \tag{19}$$

which is a scalar differential equation. $\tilde{\tilde{G}}$ can be found by evaluating the inverse transform of Eq. (18) with respect to z:

$$\tilde{\tilde{G}}\left(k_x, k_y, z\right) = \frac{1}{2\pi}\int_{-\infty}^{\infty} \frac{e^{ik_z z}}{k_z^2 + k_x^2 + k_y^2 - k^2} dk_z\,, \tag{20}$$

which is equal to

$$\tilde{\tilde{G}}\left(k_x, k_y, z\right) = \frac{e^{-u|z|}}{2u}\,, \tag{21}$$

with

$u = \left(k_x^2 + k_y^2 + k^2\right)^{1/2}$ [53].

The remaining 2D Fourier transform is

$$G(x, y, z) = \frac{1}{8\pi^2}\int_{-\infty}^{\infty}\int_{-\infty}^{\infty} \frac{1}{u}\, e^{-u|z|}\; e^{i\left(k_x x + k_y y\right)} dk_x dk_y\,. \tag{22}$$

After converting the above equation to the Hankel transform, we get

$$G(\rho, z) = \frac{1}{4\pi}\int_0^{\infty} e^{-u|z|} J_0(\lambda\rho)\, d\lambda\,, \tag{23}$$

where

$$\rho = \sqrt{x^2 + y^2}\ ,$$

$$u = \left(\lambda^2 - k^2\right)^{1/2}\text{, and}$$

$$\lambda = \left(k_x^2 + k_y^2\right)^{1/2}.$$

and J_0 is the Bessel function of the first kind of order 0. Green's function for the whole space can now be expressed by

$$G(r) = \frac{e^{-ikr}}{4\pi r}\,. \tag{24}$$

The potential vector due to a source current can be expressed by

$$\mathbf{A}(\mathbf{r}) = \int_v \frac{e^{-ik|\mathbf{r}-\mathbf{r}'|}}{4\pi|\mathbf{r}-\mathbf{r}'|}\mathbf{J}(\mathbf{r}')dv'\,, \tag{25}$$

or for an electric dipole, we can it write as

$$\mathbf{A}(\mathbf{r}) = \frac{Ids}{4\pi r}e^{-ikr}\mathbf{u}_x\,. \tag{26}$$

For a stratified 1D earth, a particular solution of a homogeneous differential equation must be added to the complementary solution in a layer containing the source dipole:

$$F_p\left(k_x, k_y\right)e^{-u_0|z+h|}, \tag{27}$$

where F_p is the incident field amplitude. The reflected field is given by

$$F_0^- = r_{TE}F_p e^{-u_0 h}\,, \tag{28}$$

where r_{TE} is the reflection coefficient given by

$$r_{TE} = \frac{Y_0 - \hat{Y}_1}{Y_0 + \hat{Y}_1} \tag{29}$$

and with

$$\hat{Y}_1 = \frac{H_y^{TE}}{E_x^{TE}} = -\frac{H_x^{TE}}{E_y^{TE}}\,, \tag{30}$$

where $\hat{Y}_1$ is the surface admittance on $z = 0$.

For an N-layered earth, as shown in Figure 1, the surface admittance and impedance are given by

$$\hat{Y}_1 = Y_1 \frac{\hat{Y}_2 + Y_1 \tanh(u_1 h_1)}{\hat{Y}_1 + Y_2 \tanh(u_1 h_1)}, \tag{31}$$

$$\hat{Y}_n = Y_n \frac{\hat{Y}_{n+1} + Y_n \tanh(u_n h_n)}{\hat{Y}_n + Y_{n+1} \tanh(u_n h_n)},$$

$$\hat{Y}_N = Y_N$$

where

$$u_n = \left(k_x^2 + k_y^2 - k_n^2\right)^{1/2}, \tag{32}$$

and

$$k_n^2 = -\hat{z}_n \hat{y}_n = \omega^2 \mu_n \varepsilon_n - i\omega\mu_n \sigma_n . \tag{33}$$

We can recursively determine $\hat{Y}_1$ from the deepest layer and consecutively iterate it upward until the surface. Between the source and the earth, the primary and secondary solutions can be combined to get the transform space as follows:

$$\tilde{F} = F_p e^{-u_0 h} \left(e^{-u_0 z} + r_{TE} e^{u_0 z}\right). \tag{34}$$

The inverse Fourier transform of the above equation is

$$F = \frac{1}{4\pi^2} \int_{-\infty}^{\infty} \int_{-\infty}^{\infty} F_p e^{-u_0 h} \left(e^{-u_0 z} + r_{TE} e^{u_0 z}\right) e^{i\left(k_x x + k_y y\right)} dk_x dk_y , \tag{35}$$

which is a function of (x,y).

Analogous with Eqs. (21) and (26) the solution for the vector potential of a horizontal electric dipole (in the x-direction) can be expressed by the 2D Fourier transform as follows:

$$\tilde{\mathbf{A}} = \frac{Ids}{2u_0} e^{-u_0(z+h)} \mathbf{u}_x ,$$

where I is the current in the dipole, and ds is the dipole length. The location of the dipole is at point z = -h on the z-axis above the earth's surface. The vector potential is calculated between the dipole and the earth.

The total electric and magnetic fields due to $\mathbf{J}^{S}_{e}$ are

$$\mathbf{E}_e = -i\omega\mu\mathbf{A} + \frac{1}{(\sigma + i\omega\varepsilon)}\nabla(\nabla\cdot\mathbf{A}) \tag{36}$$

and

$$\mathbf{H}_e = \nabla\times\mathbf{A}. \tag{37}$$

From Eqs. (36) and (37), the dipole produces the vertical component of the magnetic field expressed as

$$\tilde{H}_z^p = -\frac{\partial\tilde{A}_x}{\partial y} = -\frac{Ids}{2}\frac{ik_y}{u_0}e^{-u_0(z+h)} \tag{38}$$

To find the expression of primary TE coefficient F_p from Eq. (34), we equalize the expression of $\tilde{H}_z^p$ from Eq. (38) with

$$H_z = \frac{1}{i\omega\mu}\left(\frac{\partial^2}{\partial z^2} + k^2\right)F_z, \tag{39}$$

and finally we obtain

$$F_p = -\frac{\hat{z}_0 Ids}{2u_0}\frac{ik_y}{k_x^2 + k_y^2}. \tag{40}$$

Substituting this expression into Eq. (36) yields the expression of the TE potentials between the dipole and the earth as follows:

$$F(x,y,z) = -\frac{\hat{z}_0 Ids}{8\pi^2}\int_{-\infty}^{\infty}\int_{-\infty}^{\infty}\left[e^{-u_0(z+h)} + r_{TE}e^{u_0(z-h)}\right] \frac{ik_y}{u_0\left(k_x^2 + k_y^2\right)}e^{i\left(k_x x + k_y y\right)}dk_x dk_y \quad . \tag{41}$$

The components of the magnetic field are determined by substituting Eq. (39) into Eq. (35). The vertical magnetic field for TE potential F is expressed as

$$H_z = -\frac{Ids}{8\pi^2}\int_{-\infty}^{\infty}\int_{-\infty}^{\infty}\left(1 + r_{TE}\right)e^{u_0 z}\frac{ik_y}{u_0}e^{i\left(k_x x + k_y y\right)}dk_x dk_y, \tag{42}$$

or in the form of the Hankel transform as

$$H_z = \frac{Ids}{4\pi}\frac{y}{\rho}\int_0^{\infty}\left(1+r_{TE}\right)e^{u_0 z}\frac{\lambda^2}{u_0}J_1\left(\lambda\rho\right)d\lambda\,. \tag{43}$$

where J_1 is the Bessel function of the first kind of order 1. In this study, we performed the calculation of the Hankel transform integral denoted by Eq. (42) explicitly by using a digital linear filter based on the work of Anderson [16].

2.2 Transformation from Frequency to Time Domain

To get the value of the time domain response, we apply the inverse Laplace transform to the vertical magnetic component. The transformed field in the time domain is written as

$$h\left(t\right) = \frac{1}{2\pi i}\int_{c-\infty}^{c+\infty} H_z\left(s\right)s^{-st}ds\,, \tag{44}$$

where $H_z(s)$ is the vertical magnetic field in the Laplace domain expressed by Eq. (43). The numerical integration of Eq. (44) is executed by using the Gaver-Stehfest approximation [10-12]:

$$h\left(t\right) = \frac{\ln 2}{t}\sum_{l=2}^{L} K_l F\left(s_l\right),\ s_l = l\frac{\ln 2}{t}, \tag{45}$$

and

$$K_l = \left(-1\right)^{l+\frac{L}{2}}\sum_{k=\frac{l+1}{2}}^{\min\left(l,\frac{L}{2}\right)}\frac{k^{\frac{L}{2}}\left(2k\right)!}{\left(\frac{L}{2}-k\right)!k!\left(l-1\right)!\left(1-k\right)\left(2k-l\right)}, \tag{46}$$

where L is a coefficient number, which depends on the computer used for calculating the inverse transform. In this study, the value of L was set to 8 [13]. We are interested in $h\_(t)$, which is the transient response after the current is shut-off at $t = 0$ and is expressed as:

$$h\_\left(t\right) = h_{DC} - h\left(t\right);\ t \geq 0\,, \tag{47}$$

where h_{DC} is the induced magnetic field at $t \rightarrow \infty$ or $\omega \rightarrow 0$ due to the grounded wire source, calculated in similar fashion as $h(t)$ for layered earth, except that the value of Laplace variable s is set to zero.

In a real field measurement, a half duty cycle bipolar square wave current was injected into the ground through a grounded wire. A typical length of time for one cycle (period) related to this study was 20 s [13,24], which comprises a turn-on interval of 5 s and a turn-off interval of 5 s in alternating polarity (Figure 2). The

bipolar nature of the transmitted waveform is useful for periodic noise removal and for the determination of the transient response's zero level. A typical length of the transmitter is about 1-2 km and the transmitter-receiver offset varies from 2 to 8 km, thus ensuring that the grounded wire transmitter can be regarded as an HED. The amplitude of the injected current may vary from 15 to 25 A [13,24].

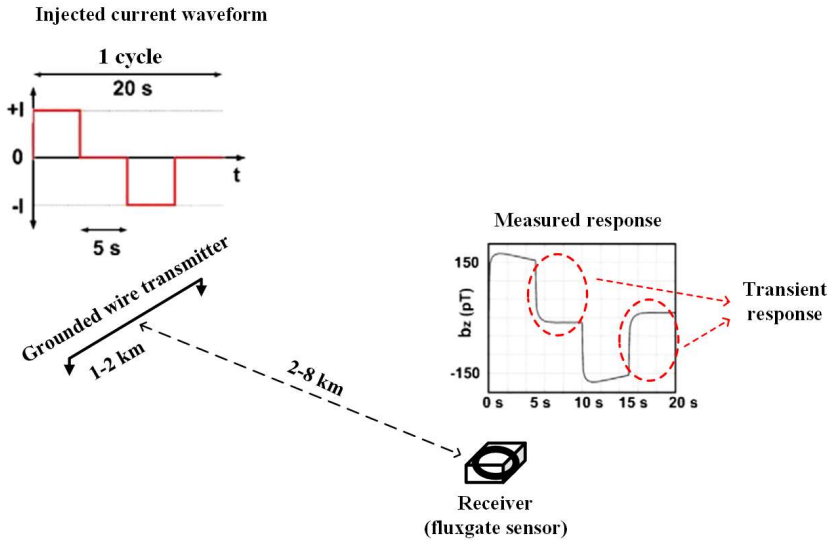

Figure 2 Illustration of the HED-TDEM setup in this study. The injected current waveform and the recorded magnetic response at the receiver site is shown here.

It is well understood that TDEM measurements conventionally use inductive coils as receivers and thus only enable us to measure the time derivative of the magnetic field (*dB/dt*). There is an inherent drawback to these measurements since they are less sensitive to the presence of good conductors. Magnetic field data that are expressed directly by *B* enhance the responses of good conductors and suppress the responses of poor conductors better than *dB/dt* data [54]. In this study, the forward expression of our data is in *B*, as we assume that fluxgate magnetometer sensors are used as receivers [13,24]. An example of an observed transient response recorded by a fluxgate magnetic sensor in the form of the vertical magnetic field component in pT is depicted in Figure 2.

3 PSO Inversion for TDEM

Farquharson and Oldenburg [55] attempted to solve the TDEM inverse problem by linearizing the nonlinear problems with an iterative re-weighted least-squares procedure. Solving grounded-wire source TDEM inversion problems by

linearization was also conducted by [56]. For a 3D case to resolve least-squares instability in the solution, [57] used the modified Gauss-Newton and applied Tikhonov regularization in solving the inversion problem. Solving the inversion problem by optimization for a TDEM sounding problem was conducted by [58] for loop and grounded-wire sources. [28] applied optimization inversion by applying simulated annealing (SA) for resistivity sounding. Ref. [59] successfully conducted the inversion by using unconstrained nonlinear optimization for 3D finite-difference and finite-element electromagnetic cases.

A powerful optimization method for solving geophysical inverse problem is by applying the PSO method [37]. In the PSO scheme, the best position of the particles and groups is evaluated by adding a function of velocity to the position of the previous particles. The velocity function is evaluated by adding the velocity of the previous particles and an acceleration-like function. The updated velocity function is expressed by the sum of weighted velocity values and the acceleration-like function. The acceleration-like function itself is expressed as the product of the PSO constants and the particle positions. The values of the weights and the PSO constants are kept small enough to ensure that the values of the updated PSO constants are significantly unchanged from the previous ones. This condition is intended for faster convergence towards best fit values while maintaining stability during the iteration of the inversion. The nonlinear inversion problem to be solved is expressed as $\mathbf{G(m)} = \mathbf{d}$, where $\mathbf{d} \in \mathbf{R}^1$ are the observed data vectors, $\mathbf{m} \in \mathbf{R}^n$ are the vector of model parameters, and $\mathbf{G}$: $\mathbf{R}^n \rightarrow \mathbf{R}^1$ is the forward function defining the physical and geometrical relations between $\mathbf{d}$ and $\mathbf{m}$. The objective function to be minimized in searching for the best value of the model parameters is determined deterministically as [60]:

$$\varepsilon\left(\mathbf{d},\delta\right) = \frac{\sum_{i=1}^{n}\left[\frac{\left(\mathbf{d}_{cal}-\mathbf{d}_{obs}\right)}{\delta}\right]^2}{n}, \tag{48}$$

where δ is the standard deviation obtained from the measured data, $\mathbf{d}_{cal}$ are the calculated data, $\mathbf{d}_{obs}$ are the observed data, and n is the number of data. The standard deviation is used to update the best particle position and the best group position to get the smallest misfit [61]. This objective function is similar to that of [62-64], except that they are not divided by the number of data.

The PSO algorithm to solve the geophysical inverse problem discussed in this study is straightforward and simple. Mainly following the works of [2,27], the implementation of the algorithm can be described as follows:

1. Defining $\mathbf{M}$, a space of models whose dimension is N and expressed as:

$$l_k \le m_{jk} \le u_k, \qquad 1 \le k \le N, \qquad 1 \le j \le N_{size}$$

where l_k and u_k are the upper and lower limits for the k-th coordinate for each model parameter (j), respectively. Each model parameter is called a particle. The particle is symbolized by a vector with the number of degrees of freedom of the inversion problem indicated by its length. Every single particle is correlated to a unique position in the search space, **M**. Search space **M** is the main prior information that is inserted into the inversion problem. In this scheme, the velocity of a particle represents the model parameter perturbations required by these particles to reach the solution of Eq. (48).

2. A swarm of particles with initial positions $\mathbf{x}_j(0)$ is randomly distributed in **M**, with a value of zero for initial velocity $\mathbf{v}_j(0)$. The forward problem $\mathbf{G}(\mathbf{x}_j(0))$ is then computed for each particle as well as misfit function $\varepsilon(\mathbf{x}_j(0))$. The values of the local and global bests for the initial swarm ($\mathbf{l}_j(0)$ and $\mathbf{g}_j(0)$) are calculated. Each particle in the N_{size} swarm undergoes the same procedure.
3. At the $(k + 1)$-th iteration, each particle in the swarm examines the search space in accordance with its misfit history $\mathbf{l}_j(k)$, and its companions' searching experience $\mathbf{g}_j(k)$ [27]:

$$\mathbf{l}_j(k) = \mathbf{x}_j(k_{bj}), \qquad \varepsilon\left(\mathbf{x}_j(k_{bj})\right) = \min_{0\le l\le k} \varepsilon\left(\mathbf{x}_j(i)\right) \tag{49}$$

$$\mathbf{g}(k) = \mathbf{l}_{j_p}(k), \qquad \varepsilon\left(\mathbf{l}_{j_p}(k)\right) = \min_{1\le j\le N_{size}} \varepsilon\left(\mathbf{l}_j(k)\right) \tag{50}$$

where *kbj* denotes the iteration for each particle *j* where the minimum misfit is achieved and *jp* is the particle in the swarm that has the minimum misfit (global best).

4. The rules for updating positions $\mathbf{x}_j(k)$ and velocities $\mathbf{v}_j(k)$ for each particle are expressed as [65-67] among others:

$$\begin{aligned} \mathbf{v}_j(k+1) &= \omega \mathbf{v}_j(k) + \phi_1 r_1 \left[\mathbf{l}_j(k) - \mathbf{x}_j(k)\right] \\ &\quad + \phi_2 r_2 \left[\mathbf{g}(k) - \mathbf{x}_j(k)\right] \\ \mathbf{x}_j(k+1) &= \mathbf{x}_j(k) + \mathbf{v}_j(k+1) \\ \phi_1 &= r_1 a_g, \ \phi_2 = r_2 a_l \end{aligned} \tag{51}$$

where ω, ϕ_1, $\phi_2 \in \mathbf{R}$ and r_1, $r_2 \in U(0,1)$. The constants ω, a_g and a_l are PSO tuning parameters, called inertia, global and local accelerations, respectively, while r_1 and r_2 are uniform random variables. Selection of the initial position $\mathbf{x}_j(k)$ significantly determines the quality of the next position after being updated [50]. Ref. [68] successfully applied the algorithm in Eq. (51) to the inversion problem of a water supply system.

4 Result and Discussion

4.1 Transformation from Frequency to Time Domain

The above PSO inversion was first applied to synthetic data generated by the forward calculation of the HED-TDEM problem for a stratified earth. The length of the HED transmitter was 1.425 km in the x-direction and the center was located at (0,0). The receiver was situated at x = 3 km and y = 4 km, giving a distance of 5 km from the center of the transmitter. A three-layer earth model was set up to generate synthetic B_z data. The resistivity values of the first, the second and the semi-infinite third layer were 25 Ωm, 1 Ωm, and 500 Ωm, respectively. The thicknesses of the first and second layers were 1000 m and 2000 m. This simple resistivity model may represent a general feature of the resistivity structure of a volcanic geothermal area comprising a resistive or moderately resistive surface layer, a conductive layer with resistivity below 10 Ωm (hydrothermally altered clay) and a third resistive layer [69,13].

In total 212 transient times and hence the same number of B_z data were calculated between 1.58 ms and 4.28 s. The resistivity model (labeled Test Model) and the generated curve of synthetic B_z (labeled Obs. Data) are depicted in Figures 3(a) and 3(b).

The total number of model parameters used in this inversion scheme was 9, comprising 5 resistivity values and 4 layer thicknesses. In this study we evaluated results from several configurations of PSO parameters to obtain the smallest misfit value, as listed in Table 1. The combinations of number of iterations and total particles were varied, whereas the maximum and minimum weight values (ω_{max} and ω_{min}) and ϕ were kept constant. It was found that a small range of ω values will give a fairly stable misfit. Relatively larger values of ω will result in greater particle velocity values as well, thus allowing the best position values of the particles to be greater. From Table 1, the lowest misfit value of 0.0089 was obtained when the combination of the number of iterations and the total number of particles was 90 and 70, respectively. Henceforth, within the scope of this study, we used this combination when performing PSO inversion, including those of field data. The comparison between the observed (synthetic) and the calculated curves of B_z using this combination is shown in Figure 3(a).

The calculated curve resembles the observed one, ensuring a very small discrepancy between them. A comparison between the resistivity test model and the inverted models is shown in Figure 3(b). The best inverted model, which is associated with the smallest misfit, consistently mimics the general pattern of the test model. However, at depth > 3000 m, the discrepancy between the test model and the inverted model is noticeable, although it is not as large as several others.

The convergence of the misfit values towards their minimum values during the increment of the iteration number is shown in Figure 3(c). Generally, for almost all combinations, misfit convergence was achieved at about the 40th iteration. Above this number, relatively small values of misfit difference and no fluctuation were observed.

Table 1 Comparison of inversion results for various combinations of PSO constants.

PSO Constants				RMS Misfit
Number of Iterations (m)	**Total Particles (n)**	**ω max/ ω min**	**Φ particle/ Φ group**	
10	10	0.3/0.2	1.2/1.2	0.7045
20	20	0.3/0.2	1.2/1.2	0.1840
30	30	0.3/0.2	1.2/1.2	0.1130
40	40	0.3/0.2	1.2/1.2	0.0320
50	50	0.3/0.2	1.2/1.2	0.0524
60	60	0.3/0.2	1.2/1.2	0.0509
70	70	0.3/0.2	1.2/1.2	0.0349
80	80	0.3/0.2	1.2/1.2	0.0548
90	90	0.3/0.2	1.2/1.2	0.0090
100	100	0.3/0.2	1.2/1.2	0.0108
90	70	0.3/0.2	1.2/1.2	0.0089

Real observed data are always accompanied by noise and the interpreted model will be affected by the presence of noise. Therefore, to test the resilience of the PSO inversion scheme to noise, 5% and 10% random noise was added to the same synthetic data. A comparison between the noisy data and the calculated data as well as the inverted models for both 5% and 10% noise are depicted in Figure 4. The RMS misfit between the 5% noisy data and the calculated data was 0.101, while that between the 10% noisy data and the calculated data was 0.537. Within the scope of this study, addition of noise increased the RMS misfit value.

The inverted models for both cases exhibited the same pattern as the test model. At shallow and intermediate depth, the model parameters (resistivity and thickness) fit those of the test model. Large discrepancies were observed at deeper depths and there were larger discrepancies for larger noise levels. These results may suggest also that there is a range of noise levels where the inverted results do not vary greatly. The stability of PSO inversion against the presence of a certain noise level in the data was also addressed by [34] in the case of using a magnetic method and [70] in the case of fitting of noisy levy data.

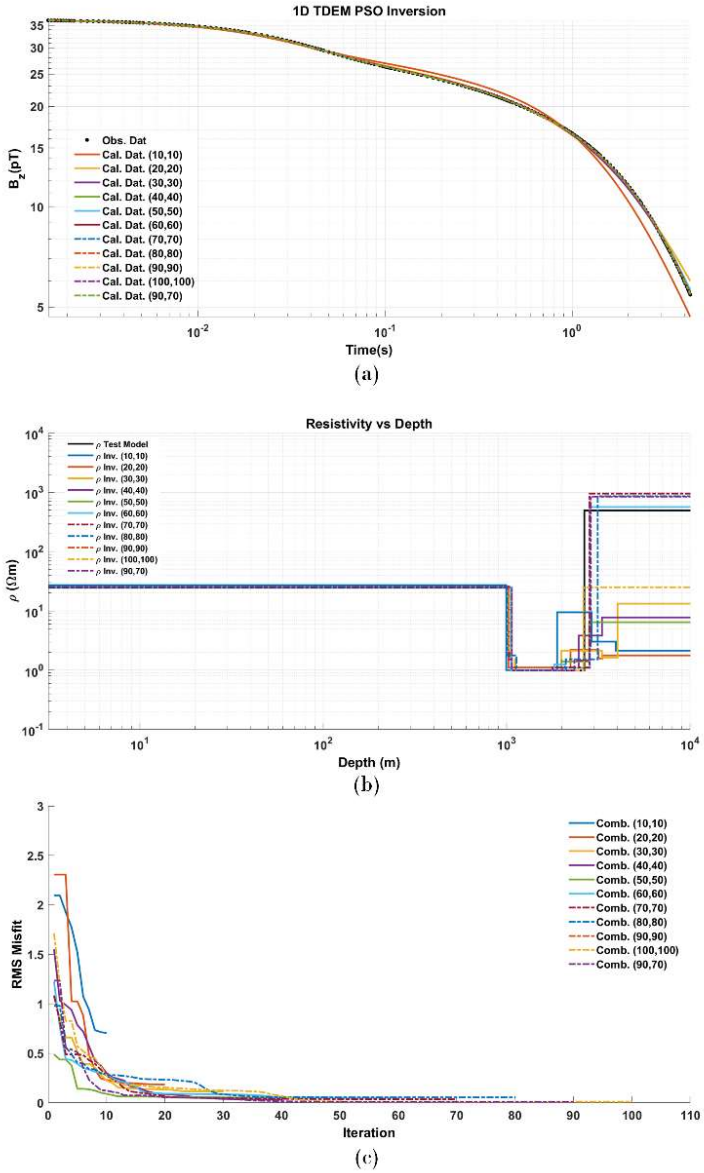

Figure 3 Inversion of synthetic data in the form of a vertical magnetic field. The numbers of particles and iterations are listed in Table 1: (a) comparison between the synthetic (observed) data and the inverted data; (b) comparison between the test model that generated the synthetic data (solid line) and the inverted resistivity models (colored lines); and (c) misfit versus number of iterations.

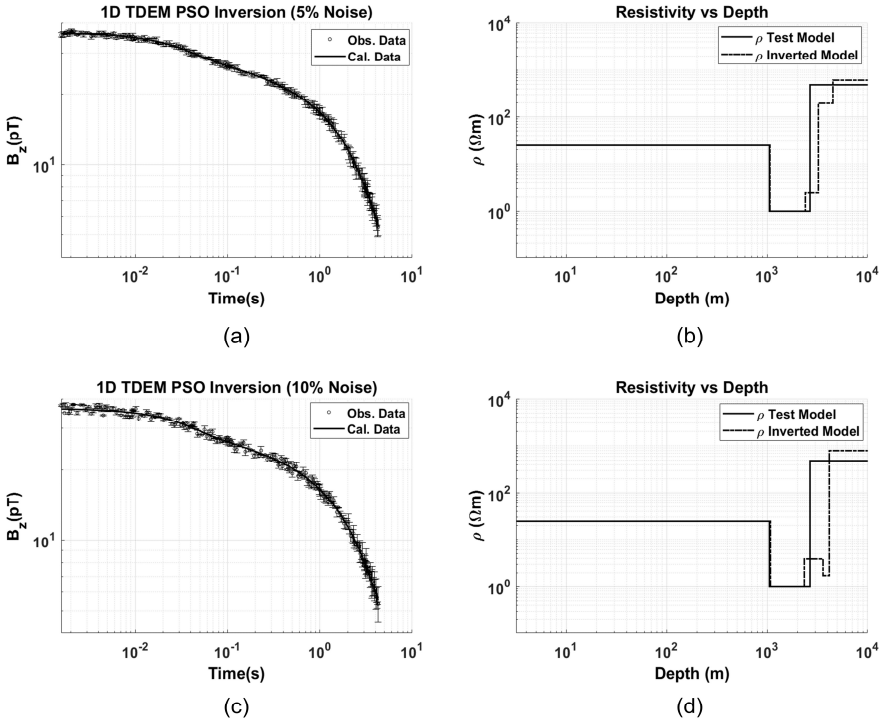

Figure 4 Addition of noise to the vertical magnetic field data and the inverted resistivity models. The combination of number of iterations and total particles was 90 and 70, respectively. (a) Comparison between 5% noisy data and the calculated data; error bars denote the standard deviations from each noise to each noise-free data. (b) Comparison between the test model and the inverted resistivity model for the data in (a). (c) Comparison between 10% noisy data and the calculated data. (d) Comparison between the test model and the inverted resistivity model for the data in (c).

4.2 Numerical Experiment with Field Data

To test its applicability in dealing with field data, the developed inversion scheme was tested on data sets recorded at two stations on the eastern flank of the Unzen volcano in Shimabara Peninsula, Kyushu Island, Japan in 2001 [13]. The two TDEM receiver stations, named UZ01 and UZ09, were located at distances of about 2 km and 4.5 km, respectively, from the center of a 1.4 km-long TDEM transmitter T_x (Figure 5). The stations were located at a fan deposit and a pyroclastic flow of the Younger Unzen complex, respectively, whose age is estimated to be 0-0.5 Ma [71].

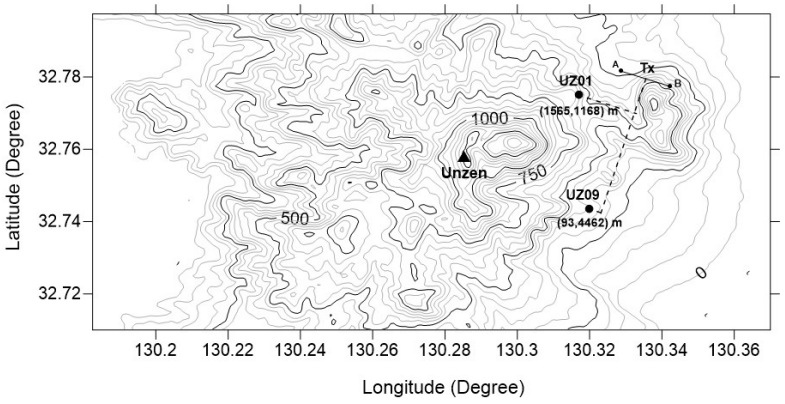

Figure 5 The (x, y) coordinates of the UZ01 and UZ02 TDEM receiver stations (in meters) relative to the center of transmitter Tx in the Unzen volcanic area, Shimabara Peninsula, Kyushu, Japan.

Figures 6(a) to (f) show a comparison between the observed and the calculated data and a comparison between the PSO inverted resistivity models and the resistivity models calculated using Occam's inversion method [62], which was applied previously to the same UZ01 and UZ09 data in [13]. Occam's inversion uses smoothness constraints, which produces a smooth resistivity model whose responses fit the observed data within an acceptable misfit tolerance. In this inversion scheme, the non-linear problem is linearized about a starting model and is solved explicitly for the deemed model instead of for a model update. During the iteration the model is parameterized by its derivative with respect to depth, ensuring the minimum norm results in the smoothest model. [13] discretized a 10-km deep subsurface into 40 layers plus one semi-infinite lowermost layer. The thicknesses of these layers were increased logarithmically with depth and were fixed, leaving only 41 resistivity values as model parameters to be estimated.

Figure 6(a) and 6(b) show a comparison between the observed data and the calculated data from PSO inversion for the UZ01 and the UZ09 station respectively. As can be seen, the fitness between the observed and the calculated data was remarkably good, except at several later transient times. These discrepancies at later times are probably caused by the nature of sites that cannot be represented by a layer and/or due to rapid decay of the data, causing a decrease in the signal-to-noise ratio of the data. The RMS misfit for UZ01 and UZ09 was about 26 and 12, respectively. These misfits differed from those of the noise-free synthetic data by about two orders of magnitude and from those of noisy synthetic data by about one order of magnitude. The PSO parameters used for inversion of the data from UZ01 and UZ09 were: total particle number 50 and 70, iteration number 50 and 90, Φ_p/Φ_g 1.2/1.2 and 2.1/2.1, $\omega_{max}/\omega_{min}$ 0.6/0.2 and 0.6/0.2, respectively.

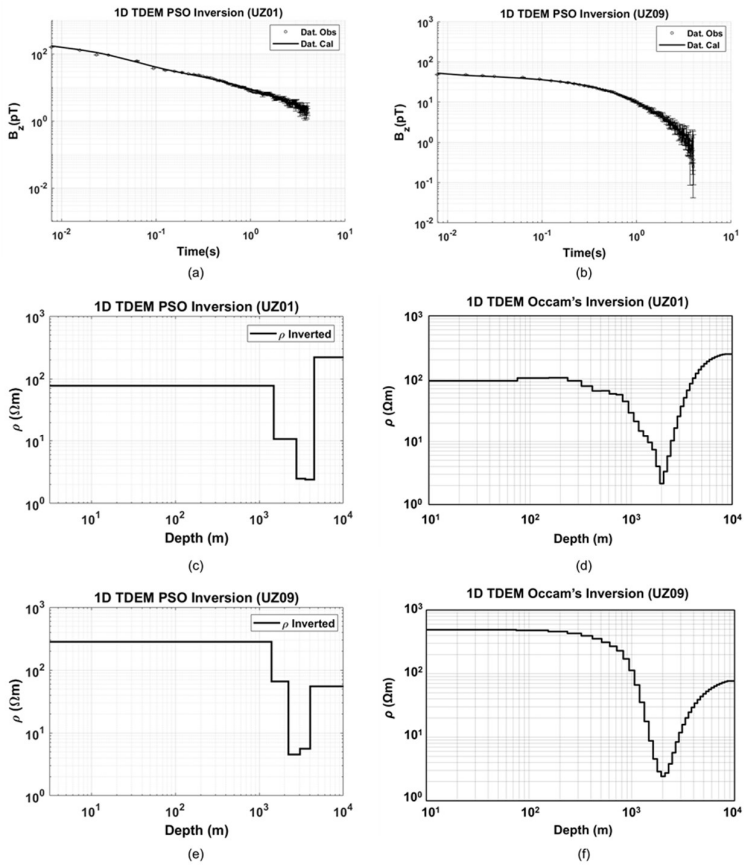

Figure 6 Comparison between observed and calculated data using the PSO inversion scheme for the (a) UZ01 data and (b) UZ09 data. Comparison between the inverted subsurface resistivity model for the UZ01 data yielded by (c) the PSO inversion (this study) and (d) Occam's inversion [13]; (e) and (f) are the same as (c) and (d) except for the data are from station UZ09.

Comparisons between the resulted models from the PSO inversion and those from Occam's inversion for UZ01 and UZ09 are depicted in Figures 6(c)-6(f). The general subsurface resistivity pattern for UZ01 resulted from the PSO inversion was the same as the pattern resulted from Occam's inversion. Both patterns show the presence of an intermediate resistive top layer of about 80-100 Ωm followed by a conductive layer of about 1-1.5 Ωm, terminated by a more resistive third layer of about 200-240 Ωm. The general feature of the resistivity profile beneath station UZ09 resulted from the PSO inversion also bore resemblance to that from Occam's inversion. A high-resistivity top layer (300-340 Ωm) overlays a

conductive layer of about 2.5-5 Ωm above a moderately resistive layer of about 50-60 Ωm. Ref. [13] suggests that conductive layers represent a combination of a water-saturated layer and hydrothermally altered rocks. The enhancement of conductivity values at the above TDEM stations may be ascribed to the supply of hot ionic gases or fluids to the water-rich layer.

5 Conclusions

A PSO inversion scheme for the HED-TDEM problem was successfully carried out for inferring subsurface resistivity models. The forward modeling part of this scheme was expressed in the Laplace domain and the inverse transformation into the time domain was conducted using the Gaver-Stehvest method. Tests to evaluate the pertinence of the PSO inversion scheme for synthetic data sets for both noise-free and noisy cases (by adding 5% and 10% random noise) revealed that this method can be a strong alternative for solving highly non-linear inverse problems such as our TDEM problem. The results also suggest that PSO inversion is relatively stable and resilient against the presence of typical noise in the data.

The algorithm of the inversion performed in this study is simple; we only need adjustment of some inversion parameters, such as inertia, acceleration coefficients and number of iteration and number of particles. Application of the inversion scheme to field data recorded at two stations in a volcanic geothermal region exhibited an excellent fit between the observed data and the calculated data, except at several later times. However, from the comparison between the models inverted by this scheme and those resulted from the deterministic smoothness-constrained Occam-type inversion, very good resemblances of the general features of the subsurface resistivity profiles were obtained. These results suggest high applicability and strong practicality of the discussed PSO inversion scheme for the non-linear HED-TDEM problem.

Acknowledgements

We would like to express our gratitude to the anonymous reviewers for their reviews and suggestions for the improvement of this manuscript. This study is partially funded by Lembaga Pengelola Dana Pendidikan (LPDP), Ministry of Finance of Republic of Indonesia in the form of a scholarship granted to one of the authors (Hapsoro) under contract no. PRJ-4570/LPDP.3/2016. The authors also wish to express their gratitude to all members of Physics of Earth and Complex Systems, Institut Teknologi Bandung, Indonesia for their kind support and permission to use the computation facility.

References

[1] Kaufman, A.A. & Keller, G.V., *Frequency and Transient Soundings*, Elsevier, Amsterdam, 1983.

[2] Ward, S.H. & Hohmann, G.W., *4. Electromagnetic Theory for Geophysical Applications*, in Electromagnetic Methods in Applied Geophysics, pp. 130-311, 1998.

[3] Nabighian, M.N. & Macnae, J.C., *6. Time Domain Electromagnetic Prospecting Methods*, in Electromagnetic Methods in Applied Geophysics, 1991.

[4] Qi, Y., Huang, L., Wu, X., Zhu, W., Fang, G. & Yu, G., *Full Wafeform Modeling of Transient Electromagnetic Response Based on Temporal Interpolation and Convolution Method*. Pure and Applied Geophysics, **176**, 2465-2477, 2019.

[5] Morisson, H.F., Phillips, R.J. & O'Brien, D.P., *Quantitative Interpolation of Transient Electromagnetic Fields of a Layered Half Space*, Geophysical Prospecting, **17**(1), pp. 82-101, 1969.

[6] Smith, R.S., *On Removing the Primary Field from Fixed-Wing Time-Domain Airborne Electromagnetic Data: Some Qonsecuences for Quantitative Modelling, Estimating Bird Position and Detecting Perfect Conductors*, Geophysical Prospecting, **49**(4), pp. 405-416, 2001.

[7] Newman, G.A., Hohmann, G.W. & Anderson, W.L., *Transient Electromagnetic Response of A Three-Dimensional Body in A Layered Earth*, Geophysics, **51(**8), pp. 1608-1627, 1986.

[8] Farquharson, C.G. & Oldenburg, D.W., *Inversion of Time-Domain Electromagnetic Data for a Horizontally Layered Earth*, Geophysical Journal International, **114**(3), pp. 433-442, 1993.

[9] Mitsuhata, Y., Murakami, Y., Uchida, T. & Amano, H., *The Fourier Transform of Controlled-Source Time-domain Electromagnetic Data by Smooth Spectrum Inversion*, Geophysical Journal International, **144**(1), pp. 123-135, 2001.

[10] Knight, J.H. & Raiche, A.P., *Transient electromagnetic calculations using the Gaver-Stehfest Inverse Laplace Transform Method*, Geophysics, **47**(1), pp. 47-50, 1982.

[11] Villinger, H., *Solving Cylindrical Geothermal Problems Using the Gaver-Stehfest Inverse Laplace Transform*, Geophysics, **50**(10), pp. 1581-1587, 1985.

[12] Kuznetsov, A., *On the Convergence of the Gaver-Stehfest Algorithm*, SIAM Journal on Numerical Analysis, **51**(6), pp. 2984-2998, 2013.

[13] Srigutomo, W., Kagiyama, T., Kanda, W., Munekane, H., Hashimoto, T., Tanaka, Y. & Utsugi, M., *Resistivity structure of Unzen Volcano derived from Time Domain Electromagnetic (TDEM) Survey*, Journal of Volcanology and Geothermal Research, **175**(1-2), pp. 231-240, 2008.

[14] Qi, Y., El-Kaliouby, H., Revil, A., Ahmed, A. S., Ghorbani, A. & Li, J., *Three-dimensional Modeling of Frequency- and Time-domain Electromagnetic Methods with Induced Polarization Effects*, Computers and Geosciences, **124**, 85-92, 2019.

[15] Qi, Y., Huang, L., Wu, X., Fang, G. & Yu, G., *Effect of Loop Geometry on TEM Response Over Layered Earth*, Pure and Applied Geophysics, **171**, pp. 2406-2415, 2014.

[16] Anderson, W.L., *Numerical Integration of related Hankel Transforms of Orders 0 and 1 by Adaptive Digital Filtering*, Geophysics, **44,** pp. 1287-1305, 1979.

[17] Fitterman, D.V. & Stewart, M.T., *Transient Electromagnetic Sounding for Groundwater*, Geophysics, **51**(4), pp. 995-1005, 1986.

[18] Zhdanov, M.S. & Pavlov, D.A., *Analysis and Interpretation of Anomalous Conductivity and Magnetic Permeability Effects in Time Domain Electromagnetic Data, Part II: Sμ-inversion*, Journal of Applied Geophysics, **46**, pp. 235-248, 2001.

[19] Qi, Y., Haung, L., Wang, X., Fang, G. & Yu, G., *Airborne Transient Electromagnetic Modeling and Inversion under Full Attitude Change,* IEEE Geoscience and Remote Sensing Letters, **14**(9), pp. 1575-1579, 2017.

[20] Blatter, D., Key, K., Ray, A., Foley, N., Tulaczyk, S. & Auken, E., *Trans-Dimensional Bayesian Inversion of Airborne Transient EM Data from Taylor Glacier, Antarctica,* Geophysical Journal International, **214**(3), pp. 1919-1936, 2018.

[21] Newman, G.A., Hohmann, G.W. & Anderson, W.L., *Transient Electromagnetic Response of a Three-Dimensional Body in a Layered Earth*, Geophysics, **51**(8), pp. 1608-1627, 1986.

[22] Asten, M.W., *Full Transmitter Waveform Transient Electromagnetic Modelling and Inversion for Sounding Over Coal Measures,* Geophysics, **52**(3), pp. 279-288, 1987.

[23] Haber, E., Oldenburg, D.W. & Shekhtman, R., *Inversion of Time Domain Three-Dimensional Electromagnetic Data,* Geophysical International Journal, **171,** pp. 550-564, 2007.

[24] Kanda, W., Utada, H., Mishina, M. & Sumitomo, N., *A Deep Transient EM Experiment in the Northern Part of Miyagi Prefecture, Northeastern Japan,* Journal of Geomagnetism and Geoelectricity, **48,** pp. 1265-1280, 1996.

[25] Gunderson, B.M., Newman, G.A. & Hohman, G.W. *Three-Dimensional Transient Electromagnetic Responses for a Grounded Source,* Geophysics, **51**(11), pp. 2117-2130, 1986.

[26] Srigutomo, W., Warsa, W., Sule, R., Trimadona, Prasetyo, D., Saito, & Widarto, D.S., *Time-domain Electromagnetic (TDEM) Baseline Survey for*

CCS in Gundih Area, Central Java, Indonesia, Proceedings of the 12th SEGJ International Symposium, Tokyo, Japan, 18-20 November, pp. 114-118, 2015.

[27] Fernández-Martínez, J.L., García-Gonzalo, E. & Naudet, V., *Particle Swarm Optimization Applied to Solving and Appraising the Streaming-Potential Inverse Problem*, Geophysics, **75**(4), pp. 1JA-Z98, 2010.

[28] Sen, M.K., Bhattacharya, B.B. & Stoffa, P.L., *Nonlinear Inversion of Resistivity Sounding Data*, Geophysics, **58**(4), pp. 496-507, 1993.

[29] Godio, A. & Santilano, A., *On the Optimization of Electromagnetic Geophysical Data: Application of the PSO Algorithm*, Journal of Applied Geophysics, **148**, pp. 163-174, 2018.

[30] Kennedy, J. & Eberhart, R., *Prognostic Evaluation of Abdominal Echography in Typhoid Fever*, Giornale Di Malattie Infettive e Parassitarie, **46**(10), pp. 1942-1948, 1994.

[31] Reynolds, C.W., *Flocks, Herds, and Schools: A Distributed Behavioral Model*, Proceedings of the 14th Annual Conference on Computer Graphics and Interactive Techniques, SIGGRAPH 1987, pp. 25-34, 1987.

[32] Eberhart, R.C. & Shi, Y., *Particle Swarm Optimization: Developments, Applications and Resources*, Proceedings of the IEEE Conference on Evolutionary Computation, ICEC, **1**, pp. 81-86, 2001.

[33] Liu, S., Liang, M. & Hu, X., *Particle Swarm Optimization Inversion of Magnetic Data: Field Examples from Iron Ore Deposits in China*, Geophysics, **83**(4), pp. J43-J59, 2018.

[34] Essa, K.S. & Elhussein, M., *PSO (Particle Swarm Optimization) for Interpretation of Magnetic Anomalies Caused by Simple Geometrical Structures*, Pure and Applied Geophysics, **175**(10), pp. 3539-3553, 2018.

[35] Essa, K.S. & Munschy, M., *Gravity Data Interpretation Using the Particle Swarm Optimisation Method with Application to Mineral Exploration,* Journal of Earth System Science, **128**(5), Article No. 123, 2019.

[36] He, M., Liu, M., Wang, R., Jiang, X., Liu, B. & Zhou, H., *Particle Swarm Optimization with Damping Factor and Cooperative Mechanism*, Applied Soft Computing Journal, **76**, pp. 45-52, 2019.

[37] Fernández Martínez, J.L., García Gonzalo, E., Fernández Álvarez, J.P., Kuzma, H. A. & Menéndez Pérez, C. O., *PSO: A Powerful Algorithm to Solve Geophysical Inverse Problems Application to a 1D-DC Resistivity Case,* Journal of Applied Geophysics, **71**(1), pp. 13-25, 2010.

[38] Pekşen, E., Yas, T. & Kıyak, A., *1-D DC Resistivity Modeling and Interpretation in Anisotropic Media Using Particle Swarm Optimization*, Pure and Applied Geophysics, **171**(9), pp. 2371-2389, 2014.

[39] Wilken, D. & Rabbel, W., *On the Application of Particle Swarm Optimization Strategies on Scholte-wave Inversion*, Geophysical Journal International, **190**(1), pp. 580-594, 2012.

[40] Poormirzaee, R., Moghadam, R.H. & Zarean, A., *Inversion seismic Refraction Data Using Particle Swarm Optimization: A Case Study of Tabriz, Iran*. Arabian Journal of Geosciences, **8**(8), pp. 5981-5989, 2015.

[41] Yang, H., Xu, Y., Peng, G., Yu, G., Chen, M., Duan, W. & Wang, X., *Particle Swarm Optimization and its Application to Seismic Inversion of Igneous Rocks*, International Journal of Mining Science and Technology, **27**(2), pp. 349-357, 2017.

[42] Xiong, J. & Zhang, T., *Multiobjective Particle Swarm Inversion Algorithm for Two-Dimensional Magnetic Data*, Applied Geophysics, **12**(2), pp. 127-136, 2015.

[43] Toushmalani, R., *Gravity Inversion of a Fault by Particle Swarm Optimization (PSO),* SpringerPlus, **2**(1), pp. 1-7, 2013.

[44] Singh, A. & Biswas, A., *Application of Global Particle Swarm Optimization for Inversion of Residual Gravity Anomalies Over Geological Bodies with Idealized Geometries*, Natural Resources Research, **25**(3), pp. 297-314, 2016.

[45] Singh, K.K. & Singh, U.K., *Application of Particle Swarm Optimization for Gravity Inversion of 2.5-D Sedimentary Basins Using Variable Density Contrast*, Geoscientific Instrumentation, Methods and Data Systems, **6**(1), pp. 193-198, 2017.

[46] Desmarais, J.K. & Spiteri, R.J., *Fast Automated Airborne Electromagnetic Data Interpretation Using Parallelized Particle Swarm Optimization*. Computers and Geosciences, **109**, pp. 268-280, 2017.

[47] Srivardhan, V., Pal, S.K., Vaish, J., Kumar, S., Bharti, A.K. & Priyam, P., *Particle Swarm Optimization Inversion of Self-potential Data for Depth Estimation of Coal Fires Over East Basuria colliery, Jharia coalfield, India,* Environmental Earth Sciences, **75**(8), Article No. 688, 2016.

[48] Chau, K. W., *Particle Swarm Optimization Training Algorithm for ANNs in Stage Prediction of Shing Mun River*, Journal of Hydrology, **329**(3-4), pp. 363-367, 2006.

[49] Fernández Martínez, J.L., Mukerji, T., García Gonzalo, E. & Suman, A., *Reservoir Characterization and Inversion Uncertainty via a Family of Particle Swarm Optimizers*, Geophysics, **77**(1), 2012.

[50] Mishra, K. K., Bisht, H., Singh, T. & Chang, V., *A Direction Aware Particle Swarm Optimization with Sensitive Swarm Leader*, Big Data Research, **14**, pp. 57-67, 2018.

[51] Yogi, I.B.S. & Widodo., *Time Domain Electromagnetic 1D Inversion Using Genetic Algorithm and Particle Swarm Optimization*, AIP Conference Proceedings, 1861, 2017.

[52] Nabighian, M.N. & Society of Exploration Geophysicists, *Electromagnetic Methods in Applied Geophysics*: *Volume 1, Theory,* Society of Exploration Geophysicists, 1988. DOI: 10.1190/ 1.9781560802631.

[53] Erdelyi, A., Ed., *Tables of Integral Transforms*, McGraw-Hill Book Co, New York, 1954.
[54] Smith, R. & Annan, P., *The Use of B-field Measurements in an Airborne Time-Domain System: Part I, Benefits of B-field versus dB/dt Data*, Exploration Geophysics, **29,** pp. 24-29, 1998.
[55] Farquharson, Colin G. & Oldenburg, D.W., *Non-linear Inversion Using General Measures of Data Misfit and Model Structure*, Geophysical Journal International, **134**(1), pp. 213-227, 1998.
[56] Sasaki, Y., *Full 3-D Inversion of Electromagnetic Data on PC*, Journal of Applied Geophysics, **46**(1), pp. 45-54, 2001.
[57] Haber, E., Oldenburg, D.W. & Shekhtman, R*., Inversion of Time Domain Three-Dimensional Electromagnetic Data,* Geophysical Journal International, **171**(2), pp. 550-564, 2007.
[58] Eaton, P.A. & Hohmann, G.W., *A Rapid Inversion Technique for Transient Electromagnetic Soundings*, Physics of the Earth and Planetary Interiors, **53**(3-4), pp. 384-404, 1989.
[59] Avdeev, D.B., *Three-Dimensional Electromagnetic Modelling and Inversion from Theory to Application*, Surveys in Geophysics, **26**, pp. 767-799, 2005.
[60] Stoffa, P.L. & Sen, M.K., *Nonlinear Multiparameter Optimization Using Genetic Algorithms: Inversion of Plane-wave Seismograms*, Geophysics, **56**(11), pp. 1794-1810, 1991.
[61] Kiran, M. S., *Particle Swarm Optimization with a New Update Mechanism*, Applied Soft Computing Journal, **60**, pp. 670-678, 2017.
[62] Menke, W., *Geophysical Data Analysis : Discrete Inverse Theory*. Academic Press Inc., 1989.
[63] Constable, S.C., Parker, R.L. & Constable, C.G., *Occam's inversion: a Practical Algorithm for Generating Smooth Models from Electromagnetic Sounding Data*, Geophysics, **52**(3), pp. 289-300, 1987.
[64] Aster, R.C., Borchers, B. & Thurber, C.H., *Parameter Estimation and Inverse Problems,* Academic Press, 2013.
[65] Shi, H., Liu, S., Wu, H., Li, R., Liu, S., Kwok, N. & Peng, Y., *Oscillatory Particle Swarm Optimizer*, Applied Soft Computing Journal, **73**, pp. 316-327, 2018.
[66] Xu, G. & Yu, G., *On Convergence Analysis of Particle Swarm Optimization Algorithm*, Journal of Computational and Applied Mathematics, **333**, pp. 65-73, 2018.
[67] Chen, Y., Li, L., Xiao, J., Yang, Y., Liang, J. & Li, T., *Particle Swarm Optimizer with Crossover Operation*, Engineering Applications of Artificial Intelligence, **70**, pp. 159-169, 2018.
[68] Montalvo, I., Izquierdo, J., Pérez, R. & Tung, M.M., *Particle Swarm Optimization Applied to the Design of Water Supply Systems*, Computers and Mathematics with Applications, **56**(3), pp. 769-776, 2008.

[69] Kagiyama, T., Utada, H. & Yamamoto, T. *Magma Ascent Beneath Unzen Volcano, SW Japan, Deduced from the Electrical Resistivity Structure,* Journal of Volcanology and Geothermal Research, **89**(1-4), pp. 35-42, 1999.

[70] Marouani, H. & Fouad, Y., *Particle Swarm Optimization Performance for fitting of Lévy Noise Data,* Physica A: Statistical Mechanics and Its Applications, **514**, pp. 708-714, 2019.

[71] Hoshizumi, H., Uto, K. & Watanabe, K., *Geology and Eruptive History of Unzen Volcano, Shimabara Peninsula, Kyushu, SW Japan*, Journal of Volcanology and Geothermal Research, **89**(1-4), pp. 81-94, 1999.